

Entropic learning enables skilful forecasts of ENSO phase at up to two years lead time

Michael Groom¹, Davide Bassetti², Illia Horenko², Terence J. O’Kane³

¹CSIRO Environment, Eveleigh, New South Wales, Australia

²Faculty of Mathematics, Rheinland-Pfälzische Technische Universität Kaiserslautern Landau, Kaiserslautern, Germany

³CSIRO Environment, Hobart, Tasmania, Australia

Key Points:

- Entropic learning can perform skilful forecasts of ENSO phase (El Niño, La Niña or neutral conditions) at up to 24 months lead time using only satellite-era observational and reanalysis data.
- The entropic learning approach effectively mitigates overfitting despite having only limited amounts of training data available, delivering probabilistic forecasts with skill comparable to the IRI ENSO prediction plume but at a small fraction of the computational cost.
- Successful hindcast validation of major ENSO events (e.g., the 2015/16 and 2018/19 El Niño events) confirms the method’s operational potential for interannual climate prediction.

arXiv:2503.01412v1 [physics.comp-ph] 3 Mar 2025

Abstract

This paper builds on previous work in applying the entropy-optimal Sparse Probabilistic Approximation (eSPA) machine learning algorithm to the task of classifying the phase of ENSO, as determined by the Niño3.4 index (Groom et al., *Artif. Intell. Earth Syst.*, 2024). In this study, only observations and reanalyses from the satellite era are employed when training and validating the entropic learning models, and a full set of hindcasts are performed over the period from 2012 to 2022 (with a maximum lead time of 24 months) in order to determine out-of-sample skill. The features used for prediction are the leading principal components from a delay-embedded EOF analysis of global sea surface temperature, the vertical derivative of temperature at the equator in the tropical Pacific (a proxy for thermocline variability) and the zonal and meridional wind stresses in the tropical Pacific.

Despite the limited number of data instances available for training (ranging from 350 monthly averages for the earliest hindcast to 520 as of December 2024), eSPA is shown to avoid overfitting in this small data regime and produces probabilistic forecasts with comparable skill to the combined (model-based) probabilistic forecasts produced from the International Research Institute for Climate and Society (IRI) ENSO prediction plume. At lead times longer than those available from the IRI plume, eSPA maintains skill out to 23 months in terms of the ranked probability skill score and 24 months in terms of the area under the Receiver Operating Characteristic curve, all at a small fraction of the computational cost of running a dynamical ensemble prediction system. Furthermore, eSPA is shown to successfully forecast the 2015/16 and 2018/19 El Niño events at 24 months lead time, the 2016/17, 2017/18 and 2020/21 La Niña events at 24 months lead time and the 2021/22 and 2022/23 La Niña events at 12 and 9 months lead time.

Plain Language Summary

This study introduces a new, cost-effective way to forecast the phase of the El Niño–Southern Oscillation (ENSO) - the dominant mode of interannual climate variability in the Pacific that alternates between El Niño, La Niña, and neutral phases - up to two years in advance using a novel machine learning method called the entropy-optimal Sparse Probabilistic Approximation (eSPA) algorithm. Despite relying solely on observational and assimilated data from satellite-era (circa 1980 onwards), eSPA overcomes the common problem of having too few historical events to learn from, as it is designed to avoid overfitting to noise in high-dimensional data. The method delivers forecasts with skill comparable to those produced by the well-established International Research Institute for Climate and Society (IRI) ENSO prediction plume, while requiring far less computing power to generate its predictions. In summary, this work demonstrates that advanced machine learning techniques can improve long-range ENSO forecasts, offering a promising tool for better preparing for the broad societal and economic impacts associated with global climate variability.

1 Introduction

Seasonal-to-interannual forecasts of the El Niño–Southern Oscillation (ENSO) are of great practical importance due to its far-reaching impacts on global weather patterns, ecosystems, and economies. However, predicting ENSO events more than 12 months in advance remains extremely challenging. Both physics-based dynamical models and statistical approaches tend to lose skill at longer lead times, especially when forecasts must cross the boreal spring predictability barrier (Barnston et al., 2012). Moreover, the short observational record (e.g. the satellite era from circa 1980 onward only contains a few strong ENSO events) means that purely data-driven models face an acute small data problem (Horenko, 2020), with only a limited number of instances of high-dimensional data to train on. These factors have contributed to the general lack of accuracy in long-range

ENSO forecasts despite decades of research. Traditionally, dynamical models have held a slight edge over statistical models for ENSO prediction on seasonal timescales. For example, an assessment by Barnston et al. (2012) on the models comprising the International Research Institute for Climate and Society (IRI) ENSO prediction plume found that dynamical models produced slightly more accurate forecasts through the boreal spring, although overall skill was low for all methods beyond about 6–9 months. Statistical models were also shown to suffer from slippage to a greater degree, which is the tendency for predicted transitions to lag observed transitions in the ENSO state due to a bias toward persistence. Tippett et al. (2012) conducted a probabilistic skill assessment of the IRI plume, using the entire multi-model ensemble to compute probabilities for each phase of ENSO (i.e., El Niño, La Niña or neutral), showing that forecasts at longer lead times fail to capture the initiation and termination of events and show the same slippage problem as the deterministic forecasts. Despite these limitations, by aggregating forecasts from the world’s leading climate prediction centres, the IRI plume remains the operational benchmark for ENSO forecasting. An up-to-date version of the plume can be found at the IRI website (https://iri.columbia.edu/our-expertise/climate/forecasts/enso/current/?enso_tab=enso-sst_table).

In recent years, the advent of deep learning has sparked a resurgence of interest in data-driven ENSO forecasting. A prominent example is the work of Ham et al. (2019), who trained a convolutional neural network (CNN) using a transfer-learning approach – first on large collections of climate model simulations from the CMIP5 ensemble, and then on ocean reanalysis data – to predict the Niño3.4 index n months ahead based on sea surface temperatures and oceanic heat content from the current and previous 2 months. This deep learning model outperformed state-of-the-art dynamical models at lead times beyond 6 months, achieving a pattern correlation with the observed index above 0.5 out to 17 months. A follow-up study applied a multitask learning framework to further improve forecast accuracy by addressing the seasonally varying nature of ENSO precursors (Ham et al., 2021). Other researchers have explored more advanced architectures and regularisation strategies to push predictive skill to even longer lead times. For instance, forecasts generated by the 3D transformer model of Zhou and Zhang (2023) were found to be skilful in predicting the Niño3.4 index at up to 18 months lead time, although biases in the training data (coming from biases in the underlying CMIP6 climate models generating the data) led to reduced skill in other regions of the Pacific. A few studies have also attempted long-range ENSO prediction using only observational and reanalysis data. Notably, Patil et al. (2023) developed a deep CNN model trained on observed/reanalysed sea surface and vertically-averaged subsurface temperatures, with skilful forecasts obtained out to 20 months lead time. Their CNN model featured multiple forms of regularisation including dropout, as well as average pooling to reduce the number of model parameters. Similar to Ham et al. (2021), it also contained heterogeneous parameters for each target season to account for seasonal variations in precursors, establishing it as a prime example of the state-of-the-art performance that is obtainable with deep learning for long-range ENSO prediction.

While these results demonstrate the promise of modern machine learning for multi-year ENSO forecasting, they also highlight persistent challenges. Many deep learning methods require “big data”, currently only obtainable through large climate model ensembles, to train models with enough parameters to capture complex spatiotemporal patterns, which can result in them inheriting some of the biases in the training data. In contrast, methods trained solely on the limited observational record risk overfitting unless they are specifically designed for the “small data” regime. To address these challenges, recent work has proposed entropic learning techniques which are based on sparsified, probabilistic approximations of the data that employ the principle of maximum entropy from information theory to avoid overfitting to noisy/uninformative features (Horenko, 2020, 2022; Vecchi et al., 2022; Horenko et al., 2023). A comparative study by Groom et al. (2024) applied the entropy-optimal Sparse Probabilistic Approximation (eSPA) classi-

fier to long-range prediction of ENSO phase and found that it can match or exceed the accuracy of deep neural networks while requiring orders of magnitude less training time and number of parameters. Building on that foundation, the present study focuses on ENSO phase forecasting using only real-time observational and reanalysis data from the satellite era, without any reliance on climate model simulations. A suite of hindcast experiments covering 2012–2022, with lead times up to 24 months, are performed to rigorously evaluate out-of-sample forecast skill, with the combined (model-based) probabilistic forecasts produced from the IRI plume employed as a benchmark.

The remainder of this paper is organised as follows. Section 2 describes the datasets, pre-processing, and the entropic learning methodology used for ENSO phase forecasting. Section 3 presents the forecasting results and comparisons with other methods, including skill assessments against standard prediction benchmarks. Section 4 discusses the implications of the findings and concludes the paper.

2 Materials and Methods

2.1 Datasets

In this study, only observations and reanalyses from the satellite era are employed when training and validating the entropic learning models. Unlike the earlier study of Groom et al. (2024), both oceanic and atmospheric fields are considered in order to give a more complete picture of the coupled dynamics of ENSO. The oceanic fields considered are monthly means of global sea surface temperature (SST) between 60°S–60°N and the vertical derivative of subsurface temperature (dT/dz) at the equator, averaged over latitudes of 5°S–5°N and restricted to longitudes of 120°E–80°W and depths of 0–500m. The atmospheric fields considered are monthly means of the zonal and meridional surface wind stresses (τ_x and τ_y), restricted to latitudes of 20°S–20°N and longitudes of 120°E–80°W, with a mask is applied so that only oceanic wind stresses are selected.

The SST data are taken from the NOAA Optimum Interpolation Sea Surface Temperature (OISST) V2.1 product (Huang et al., 2021) and are provided on a $0.25^\circ \times 0.25^\circ$ global grid. The dT/dz data are derived from potential temperature fields taken from the NOAA/NCEP Global Ocean Data Assimilation System (GODAS) reanalysis (Behringer & Xue, 2004) and are on a $1^\circ \times 1/3^\circ$ grid with 40 vertical levels. Note that SST in GODAS is strongly nudged towards the weekly OISST data with a relaxation time of 5 days (Xue et al., 2012). The wind stress data are taken from the NCEP/DOE Reanalysis 2 (NNR2) dataset (Kanamitsu et al., 2002), which provides the momentum flux, heat flux and freshwater flux forcings to GODAS, and are provided on a $2.5^\circ \times 2.5^\circ$ global grid. The combined data range from September 1981 to present day (currently December 2024), giving a total of 520 monthly averages.

2.2 Pre-processing

To calculate the Niño3.4 index, a 30-year sliding climatology is used when calculating the anomalies for a given year. This ensures that no information from the future leaks into a given hindcast and also has the desirable property that the index for a given month is uniquely defined, which is not the case when different strategies such as an expanding window are used to define the climatological period. To enable anomalies in the first 30 years of the dataset to be calculated in this manner, the sliding climatology needs to be defined by augmenting with SST data in the Niño3.4 region from earlier than September 1981. This data is taken from the NOAA Extended Reconstructed SST V5 (ERSSTv5) dataset (Huang et al., 2017).

To produce the SST and dT/dz fields the OISST and GODAS data are first regridded to a $1^\circ \times 1^\circ$ global grid using a conservative remapping and ensuring that a com-

mon land-sea mask is used. Note that while this step is not strictly necessary for this study since an EOF analysis is subsequently performed on each field separately, it allows for the possibility of using the full fields as direct inputs that are defined on a common grid in future studies. Following this, the equatorial and vertical averages/derivatives are calculated for the GODAS data. To generate the features used in each hindcast the following steps are performed, which ensure there is no leakage of future information into a given hindcast:

1. The seasonal cycle is removed by converting the data to anomalies. A base period of January 1982 to December of the year prior to the start date of the hindcast is used to define the anomalies.
2. A linear detrending step is performed prior to the EOF calculation to remove the global warming signal, where the trend is first calculated over the same base period as the anomalies and then extrapolated to times outside of this period.
3. An Empirical Orthogonal Function (EOF) analysis is performed as a dimensionality reduction step. To preserve the validity of the Euclidean distance metric, which is used both to define the reconstruction error of the principal component decomposition in EOF analysis as well as the discretisation error in eSPA, we employ the Takens (1981) delay embedding theorem and embed n lags of the data prior to constructing the covariance matrix.¹ Using a slight abuse of terminology, we refer to this procedure as Singular Spectrum Analysis (SSA) to distinguish it from conventional EOF analysis.
4. The SSA modes are calculated for the same base period of January 1982 to December of the year prior to the start date of the hindcast, then projected onto the (lagged) anomalies to give the full time series of principal components (PCs).

This procedure is then repeated for each year of hindcasts from 2012, . . . , 2022.

Following Groom et al. (2024), a fixed percentage of the total variance is used to select the number of principal components that are retained as features. For global SST, 160 PCs explaining $\sim 80\%$ of the total variance are retained, for dT/dz 140 PCs are retained explaining $\sim 90\%$ of the total variance while for the wind stresses 100 PCs are retained explaining $\sim 70\%$ of the total variance. To improve skill at short lead times, the monthly Niño3.4 index is added as a feature along with lagged values of the Niño3.4 index from the previous 6 months², bringing the total number of features used by the model to 406. Upon assembly of the feature matrix, a final pre-processing step of mapping the data to a uniform distribution with values between 0 and 1 using a quantile transformation is applied to all of the features. This is performed separately for each hindcast, which only contains data up until its given start date, thus avoiding any leakage of future information when calculating the empirical cumulative distribution function for each feature.

The targets for prediction (labels) are generated by considering the probability of the Niño3.4 index being greater than 0.5°C (El Niño), less than -0.5°C (La Niña) or neither (neutral) in n months time. For consistency with the IRI ENSO prediction plume, the 3-month running average of the Niño3.4 index is used, which along with the thresh-

¹ According to Takens' theorem, the mapping of an attractor with box-counting dimension d into the k -dimensional embedded space is diffeomorphic when $k > 2d$. In practice, it can be difficult to estimate d and therefore the embedding length n is chosen empirically by testing a range of different values. The results given in section 3 use an embedding length of 12 months, which was found to give good results while also being consistent with embedding lengths used in other studies on ENSO prediction (Zhou & Zhang, 2023) as well as capturing known optimal growth times of SST anomalies in the Pacific (Lou et al., 2021).

² An embedding length of 6 months has been shown to be sufficient for capturing the causal relationships between an index representing ENSO and its lagged values in Harries and O'Kane (2021).

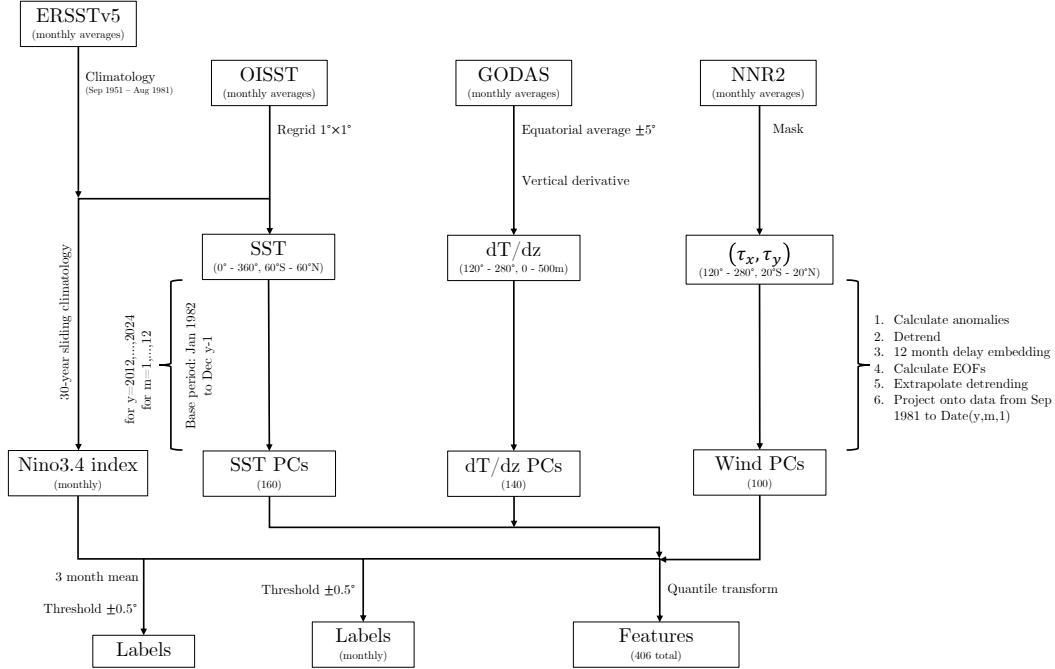


Figure 1: Summary of the data processing.

old of $\pm 0.5^\circ\text{C}$ gives class proportions of 0.25, 0.46 and 0.29 for the La Niña, neutral and El Niño classes over the period of September 1981 to December 2024. These are labelled as classes 1, 2 and 3 respectively when calculating metrics that depend on the ordinal ranking of classes such as the ranked probability score. No correction is made for the slight imbalance of classes. A summary of the data pre-processing methodology employed for generating forecasts is given in figure 1.

2.3 Entropic learning

Given the desire to use only observations and reanalyses from the satellite era, the limited number of instances available for learning (ranging from 350 for the earliest hind-cast to 520 as of December 2024) relative to the number of features (406) makes the prediction task a supervised learning problem in the small data regime where the risk of overfitting, for a given model complexity, is far greater than in typical big data applications. The recently proposed eSPA classifier has been demonstrated to cheaply and effectively avoid overfitting in this regime (Horenko, 2020; Vecchi et al., 2022) and has been thoroughly assessed on the problem of ENSO phase prediction in Groom et al. (2024). Compared to the simple out-of-sample prediction problems used in Vecchi et al. (2022); Groom et al. (2024), the formulation of the problem in this study is targeted towards the generation of real-time forecasts. This presents a number of additional impediments, many of which are due to the non-stationarity of the dynamical system we are trying to predict, that all act to reduce skill at longer lead times relative to the ideal case. Firstly, due to the inability to label instances for lead times with target dates beyond the start date of the forecast, there is an increasingly larger gap between the end of the training set and the start date of the forecast as lead time increases. The result of this is that the end of the training set becomes increasingly less relevant to the current conditions from which we are trying to generate the forecast, which is referred to as concept drift in the machine learning literature (Gama et al., 2014). Secondly, the predictions for each

lead time are all made from a single instance, i.e. the latest available monthly-averaged data. This necessitates some form of model selection, since a given model may make predictions that are otherwise correct but are incorrect for that particular instance.

We attempt to mitigate both of these issues by using an ensemble of models to generate individual predictions for each lead time and then aggregate these predictions to give a final prediction for that lead time. A more advanced aggregation strategy that leverages the interpretability of eSPA is described below in section 2.4, but prior to this an arithmetic average is used. One option for generating the ensemble is to fit eSPA models using all of the available data with different initial guesses for the model parameters, since each initial guess is guaranteed to converge to a local minimum of the loss function that will, in general, be different for different initial guesses. However, in practice we find that it is better to first split the data into a training and validation set and then fit multiple eSPA models on the training data as this also allows for hyperparameter tuning to be performed. The validation set is used to select the best model, according to a particular metric (see section 2.5 for details), across all initial guesses and hyperparameter combinations and then this process is repeated for different splits of the data until a sufficient ensemble size is generated. A total of 50 such cross-validation splits are employed, each of which is stratified by class so that the proportions of El Niño, La Niña and neutral events is the same for both training and validation sets across all splits. A train/validation split of 80%/20% was found to provide a good trade-off between a large enough training set to avoid issues of non-stationarity when training a given model and a large enough validation set to accurately assess its generalisation to unseen data.

As in Groom et al. (2024), we train separate eSPA models for each lead time of 1, 2, 3, ..., 24 months, as opposed to a single model that makes predictions for multiple lead times (i.e. multi-horizon prediction). This approach avoids the compounding of model errors at longer lead times, at the expense of having to train multiple models. With eSPA this is a worthwhile trade-off given its excellent scalability properties (being linearly scalable in the number of features D , instances T , clusters K and labels M), which make a single eSPA model very quick to train. This also allows for an easy investigation of the differences in precursors for different lead time predictions through the generation of cluster composites for SST and other fields (Groom et al., 2024). Therefore for each forecast 50 models are used for each of the 24 lead times, giving a total of 1200 models (although many more models than this are trained during the grid search for each cross-validation split).

One potential downside to this approach of using separate models to generate independent predictions for each lead time in a continuous forecast is that the predictions at subsequent lead times will not leverage any information about previous predictions that have been made at earlier lead times. Therefore, in addition to the 406 real-valued features, for a lead time of n months we provide as categorical features the class probabilities (i.e. labels) up to $n-1$ months. For the training set these will be the true labels, while for the prediction at n months ahead of the latest available data we provide the mean predictions from the ensemble that have already been made up to $n-1$ months ahead. Thus the predictions by each model at lead time n are conditioned on the sequence of class probabilities that have already been observed/predicted. This is made possible by a recent modification to eSPA that correctly accounts for categorical features. Rather than use the Euclidean distance as the clustering metric, for categorical features the Kullback-Leibler divergence is used as the appropriate measure and cluster centroids are calculated directly in the probability simplex for each feature, which represents the space of all possible probability distributions over the support of each discrete random variable. The cluster centroid for a categorical feature can be interpreted as the (normalised) geometric mean of the probability distributions assigned to that cluster.

Due to the seasonal variability in ENSO precursors, for example due to seasonal footprinting of midlatitude atmospheric variability (Vimont et al., 2003) or phase lock-

ing of the Indian Ocean Dipole (Saji et al., 1999), it is desirable to have seasonally varying model parameters that cause the model to look for different patterns in the features depending on the target season and lead time (Ham et al., 2021). One straightforward way to achieve this is to train separate models for each target season and lead time (Ham et al., 2019; Patil et al., 2023). As noted in Ham et al. (2021) there are some downsides to this approach, namely that forecast results are generated independently by separate models for each lead time, which can cause the forecast to become less consistent at longer lead times. In the present approach this is handled by the addition of categorical features from previous lead times as described in the paragraph above. Another downside is that by training separate models for each target season the amount of training data is reduced by a factor of 4, which further exacerbates the small data issue. While this may be a limiting factor for other machine learning methods, with eSPA it actually results in both improved generalisation on the validation set (in many cases the best model has a ranked probability score of exactly 0, indicating a perfect fit) as well as more skillful forecasts. This is in spite of the fact that there are now only ~ 100 instances available (prior to splitting) for training a given model. A summary of the entropic learning methodology employed for generating forecasts is given in algorithm 1.

Algorithm 1 Hindcast procedure

```

for year  $y \leftarrow 2012, \dots, 2022$  do
  for month  $m \leftarrow 1, \dots, 12$  do
    load feature matrix  $X$ 
    for lead time  $n \leftarrow 1, \dots, 24$  do
      load label matrix  $\Pi_n$ 
      for model  $i \leftarrow 1, \dots, 50$  do
        1. Add categorical features for lead times  $0, \dots, n - 1$ 
        2. Only keep instances with target month  $(m + n - 1, m + n, m + n + 1)$ 
        3. Split data into 80% train, 20% validation
        4. Grid search over hyperparameters  $K, \varepsilon_E, \varepsilon_C$ 
           return model with lowest RPS on validation set
        5. Make prediction for month  $m$ 
           return Predicted class probabilities  $\hat{\Pi}$ 
      end for
      return Average  $\hat{\Pi}$  for lead time  $n$ 
    end for
  end for
end for

```

2.4 Post-processing

Rather than use a simple arithmetic average of the model predictions at each lead time, a more advanced aggregation strategy is employed once each model in each hindcast has been trained that takes advantage of the interpretability of eSPA that was demonstrated in Groom et al. (2024). The key idea is that, by inspecting various quantities that can be derived from the affiliation matrix Γ , the cluster centroids C , the feature importance vector W and the conditional probability matrix Λ of a trained eSPA model, that model can be assigned a weight based on how likely it is deemed to be making a correct prediction for the instance corresponding to the start date of the forecast. Rather than perform this assessment manually, it is automated by framing the problem as a binary classification task where, for every single model trained over all of the hindcasts, the features are the various interpretability quantities for that model and the labels are provided by whether the model prediction corresponded to the true ENSO phase in n months time. For the full population of models trained over every hindcast (giving a total of 158,400

models), a separate eSPA model is trained to predict the probability of whether each model made a correct prediction or not. To perform hyperparameter selection while avoiding overfitting, a grid search is performed using 5-fold cross-validation with random shuffling and stratified sampling.

We refer to this new eSPA model as the meta-model, since it borrows ideas from model stacking in machine learning. Crucially however, in our approach the meta-model is not trying to improve on the predictions of the base models in the ensemble, but rather simply assign them a probability based on how likely they are deemed to be making a correct prediction using purely features relating to the base models themselves and not the underlying data they were trained on. These probabilities are used to re-weight the average over model predictions at each lead time in each hindcast, which results in an improvement in overall skill. This also provides another measure of confidence for the predictions made in a given hindcast, since lead times where none of the probabilities predicted by the meta-model are above a given threshold (e.g. $p = 0.05$) can be flagged as being low confidence. A full list of the features used as inputs for training the meta-model is given in Appendix A. Note that all of the results shown in Section 3 have been post-processed using the meta-model aggregation procedure.

2.5 Metrics

The following metrics are used both for scoring individual eSPA models as well as for assessing the ensemble predictions against ground truth data. The ranked probability score (RPS) is defined as

$$\text{RPS} = \frac{1}{T} \sum_{t=1}^T \sum_{m=1}^M \left(\sum_{j=1}^m \hat{\Pi}_{j,t} - \sum_{j=1}^m \Pi_{j,t} \right)^2, \quad (1)$$

where $\hat{\Pi}_{m,t}$ and $\Pi_{m,t}$ are the predicted and true probabilities for class $m = 1, \dots, M$ and instance $t = 1, \dots, T$ respectively. The RPS thus penalises predictions that are further away from the ground truth more heavily in cases where the classes are ordinal. Similarly, the ranked probability skill score (RPSS) is defined as

$$\text{RPSS} = 1 - \frac{\text{RPS}}{\text{RPS}_c} \quad (2)$$

where RPS_c denotes the RPS that is obtained when using climatological probabilities for the predictions (Weigel et al., 2007).

Classifier performance is also assessed through the (macro-averaged) area under the ROC curve (AUC) and expected calibration error (ECE). Here macro-averaging refers to the process of first calculating the AUC/ECE for each individual class in a one vs. rest approach and then averaging the AUCs/ECEs, weighted by their respective class priors, to get a final score. AUC is calculated by numerically integrating the curve of false positive rate vs. true positive rate (the receiver operating characteristic curve) while ECE is calculated as

$$\text{ECE} = \sum_{n=1}^N \frac{|B_n|}{T} |\text{acc}(B_n) - \text{conf}(B_n)|, \quad (3)$$

where the predicted probabilities are divided into N evenly spaced bins B_n of size $|B_n|$ (here $N = 5$ bins are used) and $\text{acc}(B_n)$ and $\text{conf}(B_n)$ are the accuracy and confidence for each bin, defined as

$$\text{acc}(B_n) = \frac{1}{|B_n|} \sum_{i \in B_n} \mathbb{1}(\hat{y}_i = y_i), \quad \text{conf}(B_n) = \frac{1}{|B_n|} \sum_{i \in B_n} \max(\hat{\Pi}_{:,i}), \quad (4)$$

with \hat{y}_i and y_i representing the predicted and true labels for instance i and $\mathbb{1}$ being an indicator function that evaluates to 1 if true and 0 otherwise. The Wilson score inter-

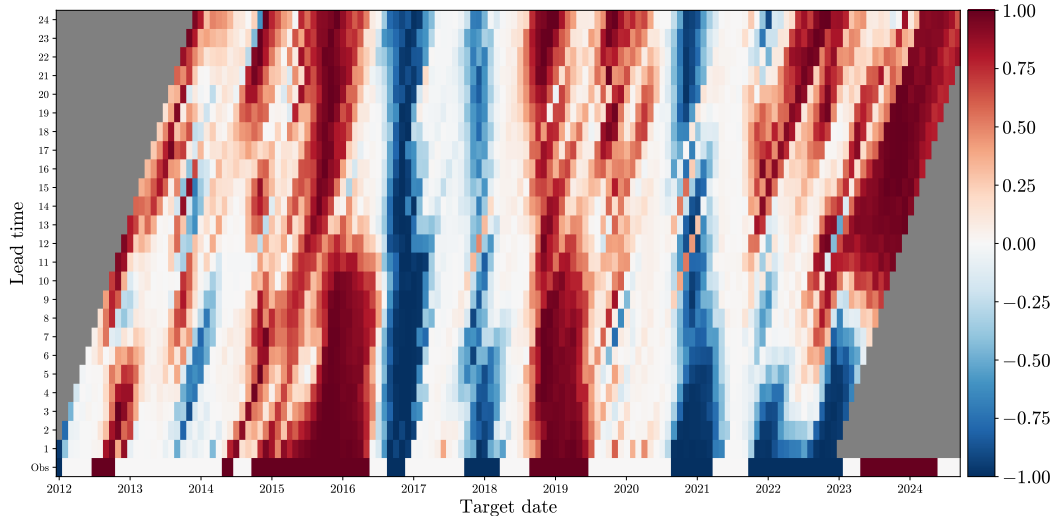


Figure 2: Expected value vs. target date and lead time.

val is used to calculate 95% confidence intervals on the AUC and bootstrapping is used to calculate 95% confidence intervals on the RPSS and ECE.

3 Results

Using the setup described in Section 2, a series of hindcasts are performed. The first hindcast has a start date of January 2012 (i.e. this is the first month to be predicted) and an end date of December 2013 while the last hindcast has a start date of December 2022 and an end date of November 2024. These hindcasts are used to assess the forecast skill according to the metrics detailed in Section 2.5, which is compared with the skill of the combined (model-based) probabilistic forecasts produced from the International Research Institute for Climate and Society (IRI) ENSO prediction plume (Tippett et al., 2012) over the same period.

3.1 Hindcasts

Figure 2 plots the results of every hindcast made between January 2012 and December 2022 using a similar convention to Figure 10 of Tippett et al. (2012). By assigning the El Niño, neutral and La Niña classes a value of 1, 0 and -1 respectively, the predicted probabilities at each lead time and target date are converted to an expected value. By comparing these expected values with the observed phase of ENSO for a given target date (as determined by the 3-month running average of the Niño3.4 index with a threshold of $\pm 0.5^\circ$), a qualitative assessment of forecast skill can be made for each of the main events during this period. In particular, we see that the 2015/16 and 2018/19 El Niño events are successfully forecast at 24 months lead time and the 2016/17, 2017/18 and 2020/21 La Niña events are also successfully forecast at 24 months lead time. The early period from 2012 to 2014 is less skilfully predicted, during which the Niño3.4 index remained almost entirely neutral. Similarly, the recent period from 2022 to 2024 which featured the 2nd and 3rd events of the "triple dip" La Niña is also less skilfully predicted, with these events only successfully forecast at 12 and 9 months lead time respectively. During the 2019-2020 period an El Niño event is incorrectly predicted for lead times of ≥ 10 months, however inspection of the Niño3.4 index during this period shows that it remained close to the threshold of 0.5° , suggesting that these longer lead forecasts are

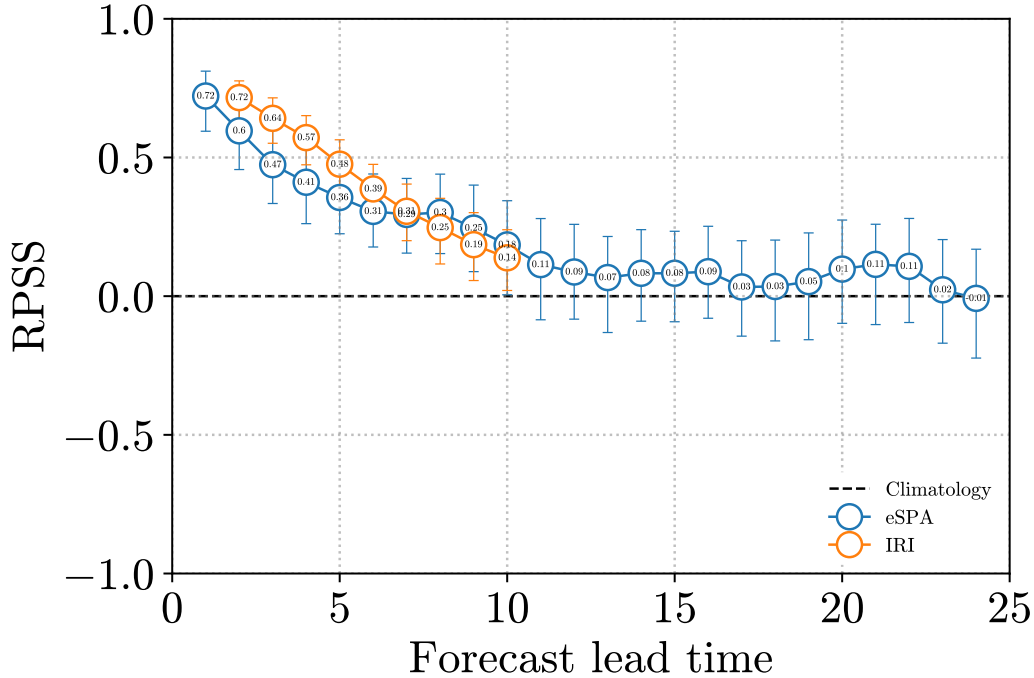


Figure 3: Ranked probability skill score vs. lead time.

not unreasonable in their predictions. Finally, the most recent 2023/24 El Niño event is shown to be successfully forecast at all lead times considered in this set of hindcasts.

Aside from the skill for individual events, the following general statements can be made regarding the performance of the eSPA-based forecasting system:

1. Unlike the categorical forecasts made by the IRI plume, the results shown in Figure 2 are largely free of "slippage", a phenomenon whereby the predictions are slow to capture the transition into and out of ENSO events, which manifests as a diagonal tilting of the target date vs. lead time plot.
2. Forecast skill for target dates during the typical peak of ENSO in boreal winter appears to be correlated with the amplitude of a given event.
3. La Niña events following an El Niño are more skillfully forecast than subsequent La Niña events.
4. The majority of incorrect predictions are between adjacent classes, i.e. El Niño and neutral or neutral and La Niña. The only period where this observation does not hold is the 2nd and 3rd events of the "triple dip" La Niña.

In the following subsections the skill over the hindcast period for both eSPA and the IRI plume will be quantified and stratified according to both lead time and target season. Note that our definition of a lead time of n months corresponds to a lead time of $n-1$ months using the IRI definition, hence the 1 month forecasts from the IRI plume are compared against our 2 month forecasts and so forth.

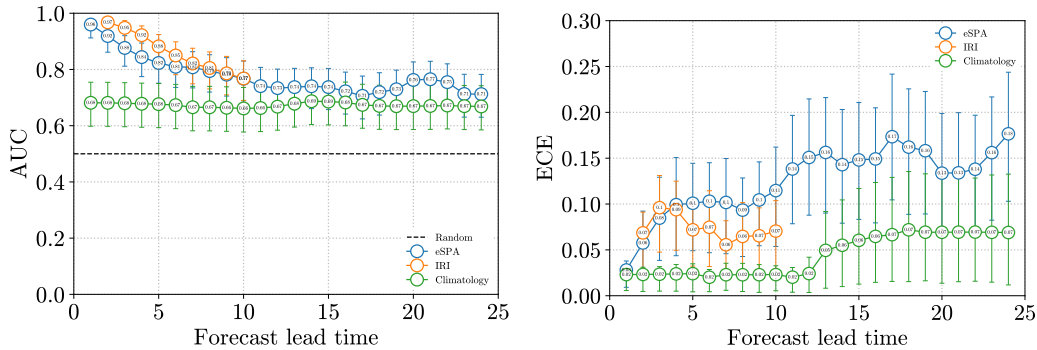


Figure 4: AUC and expected calibration error vs. lead time.

3.1.1 Skill vs. lead time

Figure 3 shows the ranked probability skill score as a function of lead time for forecasts in January 2012 to December 2022 for both eSPA and the IRI plume. By definition, a positive RPSS is skilful relative to predictions made using climatological probabilities in each target season. From this figure it can be seen that eSPA is more skilful than the IRI plume for lead times of 8 months and longer, with skill relative to climatology maintained out to 23 months. Due to the relatively small hindcast period employed in this study, these differences are not statistically significant in terms of 95% confidence intervals; only the differences between the IRI plume and climatology or eSPA and climatology out to 10 months lead time are statistically significant. We can therefore conclude that eSPA provides forecasts with similar skill as the IRI plume but at a small fraction of the total computational cost required to run each model that comprises the plume and at over twice the maximum lead time forecast published by the IRI.

Figure 4 shows two alternative metrics that are commonly used to assess classifier performance; the area under the receiver receiver operating characteristic curve (AUC) and the expected calibration error (ECE). Both of these metrics are computed as macro-averages of the AUC/ECE for each class, which are plotted in Figure 5 and Figure 6 respectively. In terms of AUC, the skill of eSPA approaches that of the IRI plume for lead times of 7 months or longer and remains skilful relative to climatology out to 24 months. As before, due to the small hindcast period the differences between eSPA and the IRI plume are not statistically significant at any lead time, while the differences between eSPA and climatology are only statistically significant for lead times up to 5 months. These conclusions also hold when looking at the individual class AUCs with the exception of the El Niño class, for which eSPA has statistically significant skill relative to climatology out to 23 months. Note that if a random classifier is used as the skill baseline, as is common in the machine learning literature, rather than climatology then eSPA is skilful at the 95% level for all lead times considered.

Another useful comparison that can be made is with the state-of-the-art CNN model of Patil et al. (2023), who also used the OISST and GODAS datasets for the validation phase (1984 to 2021) of their model. When assessing probabilistic skill, using the same threshold of $\pm 0.5^\circ$ to define each class, Patil et al. (2023) obtained AUCs of 0.69, 0.64 and 0.7 for the El Niño, Neutral and La Niña classes respectively at 24 months lead time. In comparison, eSPA obtains AUCs of 0.75, 0.67 and 0.72 respectively, albeit for a shorter assessment period. In terms of ECE, eSPA is better calibrated at earlier lead times than the IRI plume and less well-calibrated at longer ones, with none of these differences being statistically significant. Neither eSPA nor the IRI plume is as well calibrated as the

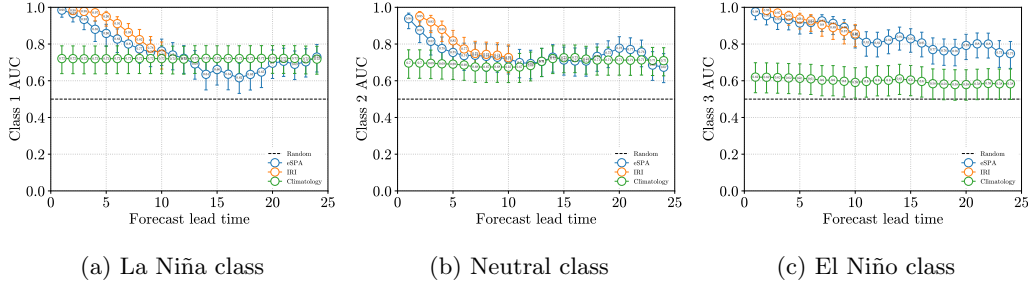


Figure 5: Class AUCs vs. lead time.

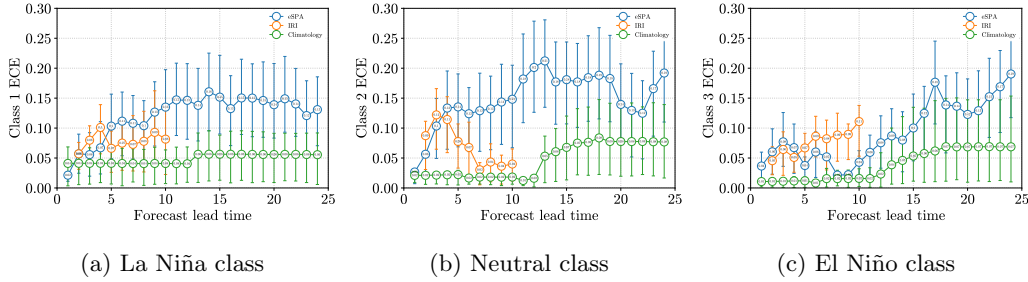


Figure 6: Class ECEs vs. lead time.

climatological probabilities, which is not surprising given that these represent the expected probabilities for each class for a given target season, and for lead times of 3-4 months and 11-12 months these differences are statistically significant. When looking at individual class ECEs, there are no significant differences between eSPA and the IRI plume for the La Niña class, while for the neutral class the IRI plume is significantly better calibrated for lead times of 7 months and longer. For the El Niño class, eSPA is better calibrated than the IRI plume for lead times of 5 months and longer, with the differences at 7 and 8 months being statistically significant.

3.1.2 Skill vs. target season

The skill vs. lead time plots in Section 3.1.1 can be further stratified by target season. A caveat to this is that, due to the small hindcast period of 11 years, each target season and lead time combination only contains 33 samples and therefore the results have large confidence intervals associated with them. Nevertheless, Figure 7 shows the RPSS for both eSPA and the IRI plume as a function of lead time and target season while Figures 8 and 9 shows the macro-averaged and individual AUCs respectively.

In terms of RPSS, there is some evidence of a boreal spring predictability barrier in both the eSPA and IRI results, although any skill barrier that does exist is much less severe than for predictions of the index directly (Barnston et al., 2012). The target season with weakest skill for eSPA is JJA, both for shorter lead times of 4-6 months and longer lead times of 20+ months. These regions of low skill are in large part due to misclassifications made for target dates in 2022 during the 2nd and 3rd successive La Niña events, which were incorrectly misclassified as El Niño at those lead times and which can be observed in Figure 2. Further examination of Figure 2 also shows that there are multiple cases where the onset of an event, which typically occurs around JJA, is missed at

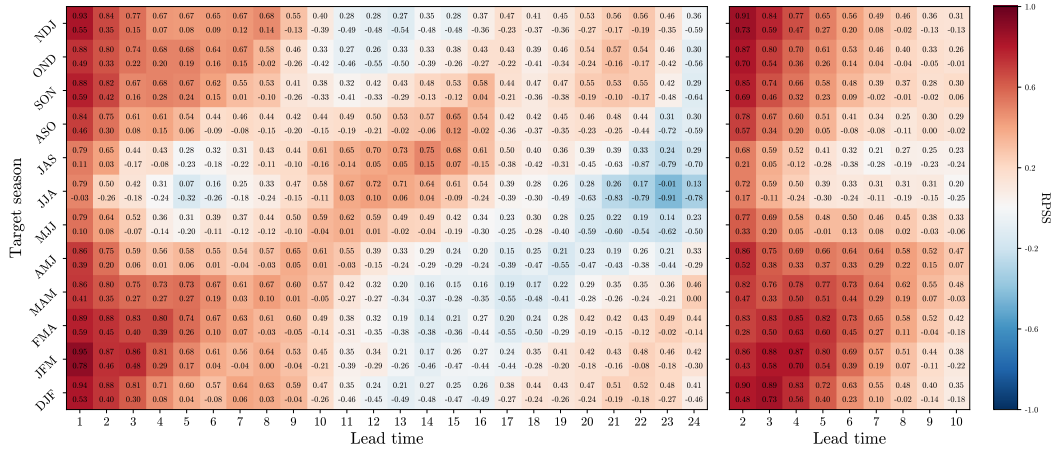


Figure 7: Ranked probability skill score vs. lead time, stratified by target season for both eSPA (left) and the IRI plume (right).

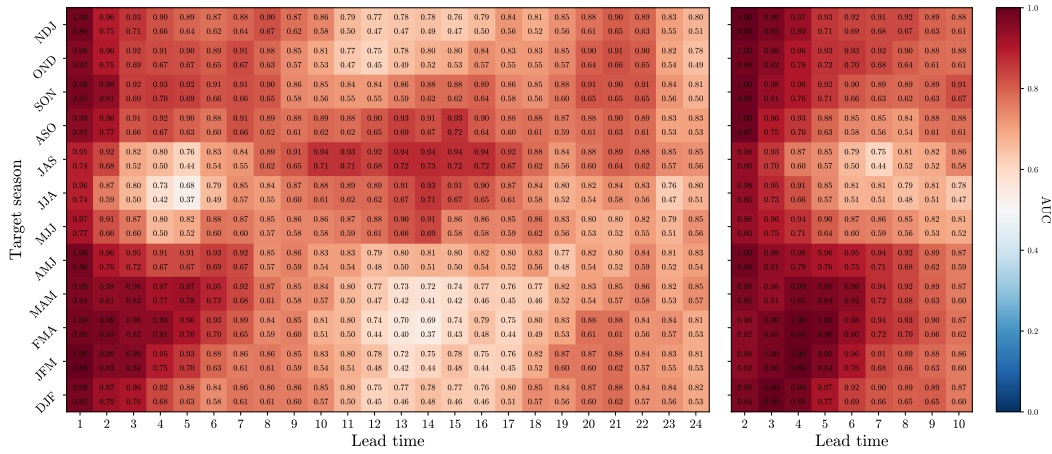
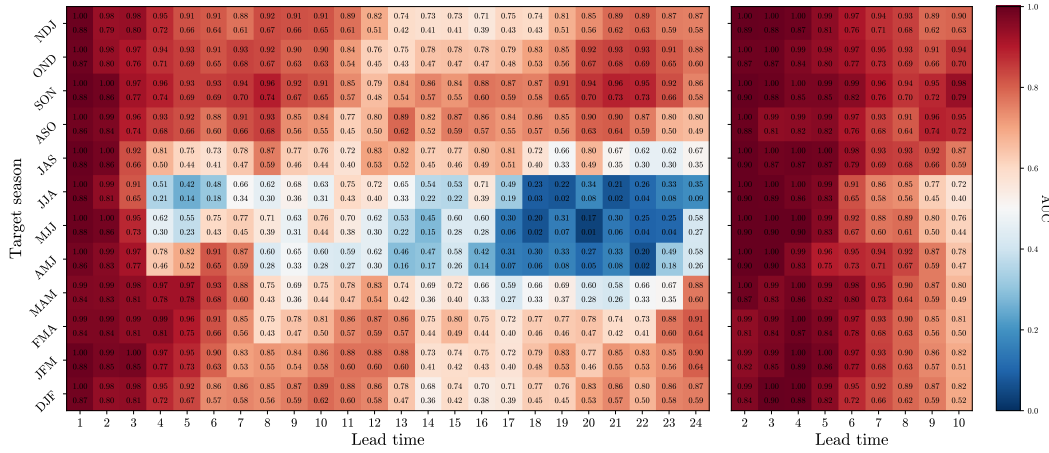


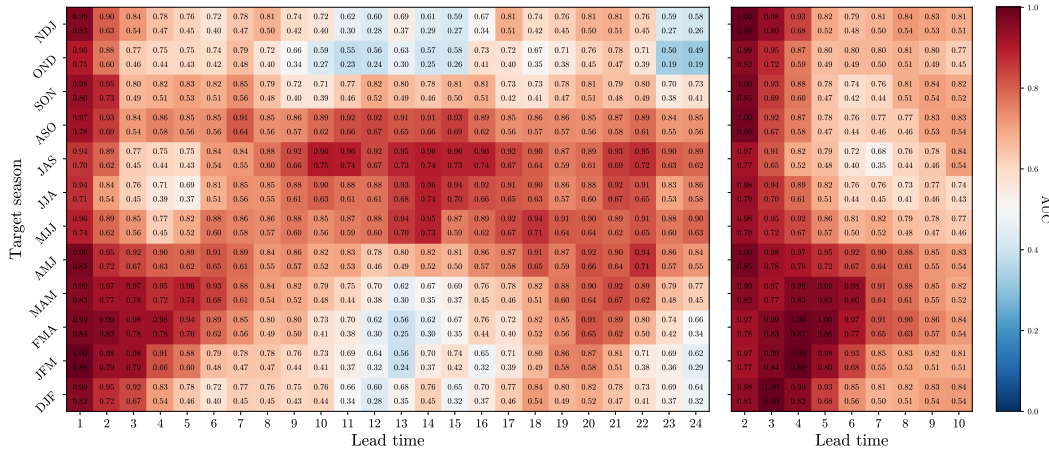
Figure 8: AUC vs. lead time, stratified by target season for both eSPA (left) and the IRI plume (right).

5 months lead time. Some possible explanations for this are that the use of monthly-averaged data filters out fast-growing modes that are necessary for correct predictions at this lead time, or that the most useful information for prediction is not contained in the provided SST, dT/dz or (τ_x, τ_y) fields at this lead time.

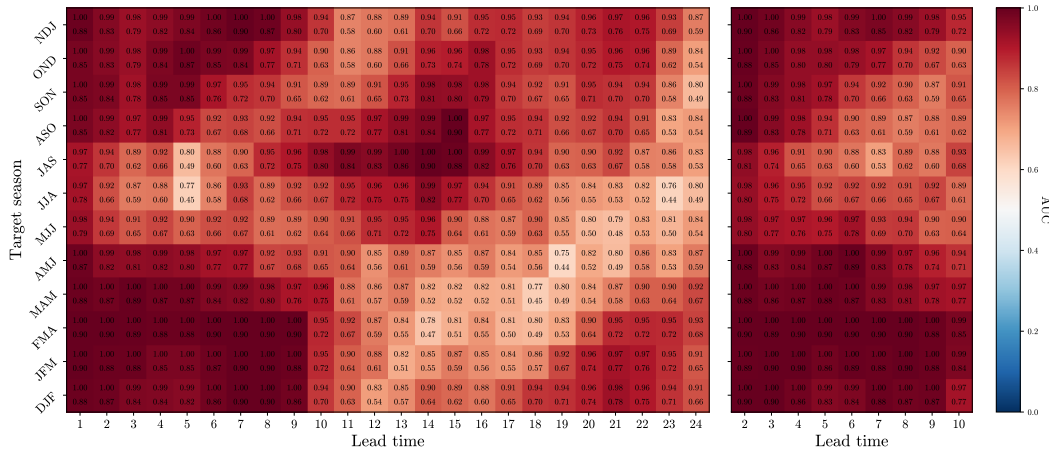
A similar phenomenon is seen in Figure 8 for the AUC, which is further decomposed by individual classes in Figure 9. In particular, Figure 9 shows that the drop in AUC for JJA at 4-6 months lead time is mostly due to misclassification made for the La Niña class. However, it is important to highlight that there is only 1 instance of a La Niña occurring during JJA for this hindcast period. Therefore the lack of skill for that particular event may not translate to a general lack of skill at that target season and lead time.



(a) La Niña class



(b) Neutral class



(c) El Niño class

Figure 9: Class AUCs vs. lead time, stratified by target season for both eSPA (left) and the IRI plume (right).

4 Conclusions

This paper has demonstrated the effective application of the entropy-optimal Sparse Probabilistic Approximation (eSPA) algorithm to long-range forecasting of ENSO phase. The eSPA classifier predicts whether the Niño3.4 index will be in El Niño, La Niña, or neutral conditions at a given lead time using a set of features derived from a delay-embedded EOF analysis of global sea surface temperatures, subsurface thermocline proxies and surface wind stresses in the tropical Pacific. In contrast to prior work (Groom et al., 2024), a large ensemble of eSPA models were trained and validated exclusively on observational and reanalysis data from the post-1980 satellite era, with great care taken to avoid any form of information leakage from the future into the training set. A series of hindcast experiments were conducted for start dates from January 2012 to December 2022 at lead times of 1 up to 24 months in order to assess forecast skill. A state-of-the-art multi-model forecast ensemble – the International Research Institute (IRI) ENSO prediction plume – was employed as a benchmark for skill evaluation.

A key strength of the entropic learning framework is its interpretability and diagnostic insight. In contrast to black-box deep learning models, eSPA provides transparent probabilistic relationships between observed features and ENSO variability. In this study, these interpretable outputs were exploited to design a novel ensemble aggregation strategy. Rather than weighting all ensemble members equally, the internal structure of each individual eSPA model in the ensemble was used to gauge the likelihood of its prediction being correct and re-weight its contribution to the overall prediction at that lead time. This meta-learning approach effectively learns to “predict the likelihood of the predictions”, boosting overall forecast performance and offering a practical example of how explainable machine learning can be harnessed in climate forecasting.

Despite the limited number of training instances (on the order of only a few hundred monthly samples for each hindcast), eSPA achieved skillful performance across all forecast lead times considered. At lead times overlapping with those published for the IRI plume (up to 10 months), eSPA attained predictive skill with statistically insignificant differences at the 95% confidence level. Moreover, at extended lead times beyond the range of the IRI operational forecasts, eSPA maintained positive skill out to 23 months in terms of ranked probability skill score and out to 24 months in terms of area under the ROC curve (AUC). This performance effectively doubles the forecast horizon of conventional ENSO outlooks, as the IRI and other operational systems typically issue projections only up to about one year ahead. Notably, eSPA demonstrated the capability to anticipate major ENSO events during the hindcast period well in advance; the 2015/16 and 2018/19 El Niño events were successfully predicted at 24 months lead time, as were the 2016/17, 2017/18 and 2020/21 La Niña events. Furthermore, these forecasts are achieved at a small fraction of the computational cost required by conventional dynamical models, underscoring the efficiency of our entropic learning framework for near-term climate prediction. In addition, comparisons with other machine learning-based forecasting methods indicate that the present approach is highly competitive. For instance, the AUC obtained by eSPA at the 24-month lead time exceeds that reported for the recent deep convolutional neural network of Patil et al. (2023) which was trained on similar data, highlighting the advantages of the proposed approach even relative to state-of-the-art deep learning models.

Given the promising results presented in this work there are several avenues for future research and development, a few of which are highlighted here. Firstly, there is the potential to adapt the framework to directly predict the Niño3.4 index in a regression setting (e.g. via the SPARTAN algorithm presented in Horenko et al. (2023)), which may provide additional performance benefits for forecasting ENSO phase due to the ordering of targets being naturally enforced in the problem formulation. Such a system should be evaluated with rigorous hindcast experiments in the same manner as this study. A second useful extension would be to train multiple eSPA/SPARTAN models on differ-

ent segments or regimes of the historical record, within an adaptive regime-learning framework that is able to handle non-stationarity in the climate system due to interdecadal variability and anthropogenic forcing. This approach could help maintain skill during challenging periods, such as the recent 2022-2023 period, by allowing the forecasting system to adjust to varying background conditions. Seasonal variability in predictors could also be handled in a similar manner, e.g. using the temporally-regularised eSPA method presented in Bassetti et al. (2024), avoiding the need to restrict the training data for each model to only those instances in the given target season. Finally, the methodology developed here may be applied to other modes of climate variability beyond ENSO. In particular, deploying the entropic learning framework to forecast intraseasonal phenomena such as the Madden-Julian Oscillation, or extending it to multiple outputs for simultaneous prediction of both ENSO and the Indian Ocean Dipole (Ling et al., 2022) are important next steps. Pursuing these directions could pave the way toward a unified, data-driven model of intraseasonal to interannual tropical climate variability and improve our understanding of predictability across different timescales as well as interactions between different modes that lead to compound events.

Appendix A Features used to train the meta-model

A given base eSPA model consists of a $K \times T$ affiliation matrix Γ , a $D \times K$ matrix of cluster centroids C , a $M \times K$ matrix of conditional probabilities Λ and a D -dimensional feature importance vector W , as well as a $M \times T'$ array of predictions $\hat{\Pi}$ where T' is the number of unlabelled instances. These matrices/vectors are used to derive the following real-valued features that are supplied as inputs to the meta-model (where t corresponds to the most recent unlabelled instance and k denotes the cluster that instance has been assigned to):

1. The difference between the true monthly-averaged Niño3.4 index at time t (i.e. the start date of the forecast) and the Niño3.4 index calculated from the SST anomaly composite corresponding to cluster k . Note: only the 0-months lag field from the SST composite is considered.
2. The RMSE between the true monthly-averaged Niño3.4 index from times $t-11, \dots, t$ and the Niño3.4 index calculated from the SST anomaly composite corresponding to cluster k . Note: all fields from the SST composite are considered, corresponding to 12 time snapshots.
3. The pattern correlation between the true monthly-averaged Niño3.4 index from times $t-11, \dots, t$ and the Niño3.4 index calculated from the SST anomaly composite corresponding to cluster k . Note: all fields from the SST composite are considered, corresponding to 12 time snapshots.
4. The (area-weighted) RMSE between the true monthly-averaged SST anomaly field at time t and the SST anomaly composite corresponding to cluster k , restricted to the tropical Pacific (20°S-20°N and 120°E-80°W). Note: only the 0-months lag field from the SST composite is considered.
5. The (area-weighted) pattern correlation between the true monthly-averaged SST anomaly field at time t and the SST anomaly composite corresponding to cluster k , restricted to the tropical Pacific (20°S-20°N and 120°E-80°W). Note: only the 0-months lag field from the SST composite is considered.
6. The (area-weighted) RMSE between the true monthly-averaged dT/dz anomaly field at time t and the dT/dz anomaly composite corresponding to cluster k , restricted to the tropical Pacific (120°E-80°W). Note: only the 0-months lag field from the dT/dz composite is considered.
7. The (area-weighted) pattern correlation between the true monthly-averaged dT/dz anomaly field at time t and the dT/dz anomaly composite corresponding to cluster k , restricted to the tropical Pacific (120°E-80°W). Note: only the 0-months lag field from the dT/dz composite is considered.

8. The (area-weighted) RMSE between the true monthly-averaged wind stress anomaly field at time t and the wind stress anomaly composite corresponding to cluster k , restricted to the tropical Pacific (20°S-20°N and 120°E-80°W). Note: only the 0-months lag field from the wind stress composite is considered.
9. The (area-weighted) pattern correlation between the true monthly-averaged wind stress anomaly field at time t and the wind stress anomaly composite corresponding to cluster k , restricted to the tropical Pacific (20°S-20°N and 120°E-80°W). Note: only the 0-months lag field from the wind stress composite is considered.
10. A binary variable indicating whether the Niño3.4 index calculated from the SST anomaly composite corresponding to cluster k is in the same phase as the true monthly-averaged Niño3.4 index at time t . Note: only the 0-months lag field from the SST composite is considered.
11. A binary variable indicating whether the composite generated by averaging over the SST anomaly field for all instances that appear n months ahead of those instances assigned to cluster k has a Niño3.4 index that is in the same phase as the majority class of the predicted label $\hat{\Pi}(:, t)$ for lead time n .
12. The distance on the probability simplex between the predicted label $\hat{\Pi}(:, t)$ and the extremised predicted label $\tilde{\Pi}(:, t)$, which is calculated as

$$\tilde{\Pi}(m, t) = \begin{cases} 1 & \text{if } m = \operatorname{argmax}(\hat{\Pi}(:, t)) \\ 0 & \text{otherwise} \end{cases}$$

13. The Euclidean distance between the (pre-processed) feature vector $X(:, t)$ and the cluster centroid $C(:, k)$.
14. The weighted Euclidean distance between the (pre-processed) feature vector $X(:, t)$ and the cluster centroid $C(:, k)$, weighted by W .
15. The minimal adversarial distance (Horenko, 2023) from instance t to a cluster k' where $\Lambda(m, k') \leq 1/3$ and $m = \operatorname{argmax}(\hat{\Pi}(:, t))$.
16. The (two-tailed) p -value for cluster k that is calculated by forming a contingency table between $\Gamma_{k,:}$ and $\Pi_{m,:}$ for each m and using Fisher's exact test to calculate the probability of observing this particular arrangement of the data under the null hypothesis that either value of the label m (i.e. 0 or 1) is likely to be present in the instances assigned to cluster k . The p -value that is returned for each cluster is the one corresponding to the label with the highest conditional probability (given by $\operatorname{argmax}(\Lambda_{:,k})$).
17. The fraction of clusters \tilde{K} that have a p -value < 0.05 .
18. The proportion of features \tilde{D} whose feature importance is greater than the maximum entropy limit of $1/D$.
19. The total weight in W assigned to real-valued features.
20. The number of consecutive times that the predicted class m has been predicted / previously occurred.
21. The number of instances in the training set that are assigned to cluster k , normalised by T .
22. The ranked probability score for the training set.
23. The ranked probability score for the validation set.

In addition, the following categorical features are also supplied as inputs to the meta-model:

1. The predicted probabilities $\hat{\Pi}(:, t)$.
2. The predicted probabilities $\hat{\Pi}(:, t - 1)$.
3. The climatological probabilities for the month corresponding to the target month $t + n$.
4. The average predicted probabilities for all 50 models with the same start date and lead time n .

5. The average predicted probabilities for all 50 models with the same start date and lead time $n - 1$. If $n = 1$ this is set to the true label on the start date.
6. The average predicted probabilities corresponding to the start of the sequence of all consecutive predictions with $\text{argmax}(\hat{\Pi}(:, t)) = m$. This is set to the true label on the start date if the sequence extends all the way back to $n = 0$.

References

- Barnston, A. G., Tippett, M. K., L'Heureux, M. L., Li, S., & DeWitt, D. G. (2012, May). Skill of Real-Time Seasonal ENSO Model Predictions During 2002–11: Is Our Capability Increasing? *Bulletin of the American Meteorological Society*, *93*(5), ES48–ES50. Retrieved 2023-12-07, from <https://journals.ametsoc.org/doi/10.1175/BAMS-D-11-00111.2> doi: 10.1175/BAMS-D-11-00111.2
- Bassetti, D., Pospíšil, L., & Horenko, I. (2024, June). On Entropic Learning from Noisy Time Series in the Small Data Regime. *Entropy*, *26*(7), 553. Retrieved from <https://www.mdpi.com/1099-4300/26/7/553> doi: 10.3390/e26070553
- Behringer, D. W., & Xue, Y. (2004). Evaluation of the global ocean data assimilation system at ncep: The pacific ocean. In *Eighth symp. on integrated observing and assimilation system for atmosphere, ocean, and land surface*.
- Gama, J., Zliobaite, I., Bifet, A., Pechenizkiy, M., & Bouchachia, A. (2014). A survey on concept drift adaptation [Review]. *ACM Computing Surveys*, *46*(4). Retrieved from <https://www.scopus.com/inward/record.uri?eid=2-s2.0-84901228061&doi=10.1145%2f2523813&partnerID=40&md5=d02bb1b645cabca78b8ea4a25eff5de> (Cited by: 2173; All Open Access, Green Open Access) doi: 10.1145/2523813
- Groom, M., Bassetti, D., & Horenko, I. (2024). On the Comparative Utility of Entropic Learning versus Deep Learning for Long-Range ENSO Prediction. *Artif. Intell. Earth Syst.*, *3*, 240009.
- Ham, Y.-G., Kim, J.-H., Kim, E.-S., & On, K.-W. (2021, July). Unified deep learning model for El Niño/Southern Oscillation forecasts by incorporating seasonality in climate data. *Science Bulletin*, *66*(13), 1358–1366. Retrieved 2024-01-16, from <https://linkinghub.elsevier.com/retrieve/pii/S2095927321002243> doi: 10.1016/j.scib.2021.03.009
- Ham, Y.-G., Kim, J.-H., & Luo, J.-J. (2019). Deep learning for multi-year ENSO forecasts. *Nature*, *573*(7775), 568–572.
- Harries, D., & O’Kane, T. J. (2021). Dynamic Bayesian Networks for Evaluation of Granger Causal Relationships in Climate Reanalyses. *Journal of Advances in Modeling Earth Systems*, *13*(5), e2020MS002442. doi: 10.1029/2020MS002442
- Horenko, I. (2020, August). On a Scalable Entropic Breaching of the Overfitting Barrier for Small Data Problems in Machine Learning. *Neural Computation*, *32*(8), 1563–1579. Retrieved 2023-03-14, from <https://doi.org/10.1162/neco.a.01296> doi: 10.1162/neco.a.01296
- Horenko, I. (2022). Cheap robust learning of data anomalies with analytically solvable entropic outlier sparsification. *Proceedings of the National Academy of Sciences*, *119*(9), e2119659119. doi: 10.1073/pnas.2119659119
- Horenko, I. (2023). *On existence, uniqueness and scalability of adversarial robustness measures for AI classifiers*. arXiv. Retrieved from <http://arxiv.org/abs/2310.14421> doi: 10.48550/arXiv.2310.14421
- Horenko, I., Vecchi, E., Kardoš, J., Wächter, A., Schenk, O., O’Kane, T. J., . . . Gerber, S. (2023, January). On cheap entropy-sparsified regression learning. *Proceedings of the National Academy of Sciences*, *120*(1), e2214972120. Retrieved 2023-06-08, from <https://pnas.org/doi/10.1073/pnas.2214972120> doi: 10.1073/pnas.2214972120
- Huang, B., Liu, C., Banzon, V., Freeman, E., Graham, G., Hankins, B., . . . Zhang, H.-M. (2021). Improvements of the daily optimum interpolation sea surface

- temperature (doisst) version 2.1. *Journal of Climate*, *34*(8), 2923 - 2939. Retrieved from <https://journals.ametsoc.org/view/journals/clim/34/8/JCLI-D-20-0166.1.xml> doi: 10.1175/JCLI-D-20-0166.1
- Huang, B., Thorne, P. W., Banzon, V. F., Boyer, T., Chepurin, G., Lawrimore, J. H., ... Zhang, H.-M. (2017). Extended reconstructed sea surface temperature, version 5 (ersstv5): Upgrades, validations, and intercomparisons. *Journal of Climate*, *30*(20), 8179 - 8205.
- Kanamitsu, M., Ebisuzaki, W., Woollen, J., Yang, S.-K., Hnilo, J. J., Fiorino, M., & Potter, G. L. (2002). Ncep-doe amip-ii reanalysis (r-2). *Bulletin of the American Meteorological Society*, *83*(11), 1631 - 1644. Retrieved from <https://journals.ametsoc.org/view/journals/bams/83/11/bams-83-11-1631.xml> doi: 10.1175/BAMS-83-11-1631
- Ling, F., Luo, J.-J., Li, Y., Tang, T., Bai, L., Ouyang, W., & Yamagata, T. (2022, December). Multi-task machine learning improves multi-seasonal prediction of the Indian Ocean Dipole. *Nature Communications*, *13*(1), 7681. Retrieved 2023-12-08, from <https://www.nature.com/articles/s41467-022-35412-0> doi: 10.1038/s41467-022-35412-0
- Lou, J., O’Kane, T. J., & Holbrook, N. J. (2021, October). Linking the atmospheric Pacific-South American mode with oceanic variability and predictability. *Communications Earth & Environment*, *2*(1), 223. Retrieved 2024-03-19, from <https://www.nature.com/articles/s43247-021-00295-4> doi: 10.1038/s43247-021-00295-4
- Patil, K. R., Doi, T., Jayanthi, V. R., & Behera, S. (2023, January). Deep learning for skillful long-lead ENSO forecasts. *Frontiers in Climate*, *4*, 1058677. Retrieved 2023-12-08, from <https://www.frontiersin.org/articles/10.3389/fclim.2022.1058677/full> doi: 10.3389/fclim.2022.1058677
- Saji, N. H., Goswami, B. N., Vinayachandran, P. N., & Yamagata, T. (1999, September). A dipole mode in the tropical Indian Ocean. *Nature*, *401*(6751), 360–363. Retrieved 2024-11-13, from <https://www.nature.com/articles/43854> doi: 10.1038/43854
- Takens, F. (1981). Detecting strange attractors in turbulence. In D. Rand & L.-S. Young (Eds.), *Dynamical systems and turbulence, warwick 1980* (pp. 366–381). Berlin, Heidelberg: Springer Berlin Heidelberg.
- Tippett, M. K., Barnston, A. G., & Li, S. (2012). Performance of Recent Multimodel ENSO Forecasts. *Journal of Applied Meteorology and Climatology*, *51*(3), 637–654. doi: 10.1175/JAMC-D-11-093.1
- Vecchi, E., Pospíšil, L., Albrecht, S., O’Kane, T. J., & Horenko, I. (2022, April). eSPA+: Scalable Entropy-Optimal Machine Learning Classification for Small Data Problems. *Neural Computation*, *34*(5), 1220–1255. Retrieved 2023-03-14, from <https://doi.org/10.1162/neco.a.01490> doi: 10.1162/neco.a.01490
- Vimont, D. J., Wallace, J. M., & Battisti, D. S. (2003). The seasonal footprinting mechanism in the pacific: Implications for enso. *Journal of Climate*, *16*(16), 2668 - 2675. doi: 10.1175/1520-0442(2003)016<2668:TFSFMIT>2.0.CO;2
- Weigel, A. P., Liniger, M. A., & Appenzeller, C. (2007, January). The Discrete Brier and Ranked Probability Skill Scores. *Monthly Weather Review*, *135*(1), 118–124. Retrieved 2024-11-21, from <http://journals.ametsoc.org/doi/10.1175/MWR3280.1> doi: 10.1175/MWR3280.1
- Xue, Y., Balmaseda, M. A., Boyer, T., Ferry, N., Good, S., Ishikawa, I., ... Yin, Y. (2012). A comparative analysis of upper-ocean heat content variability from an ensemble of operational ocean reanalyses. *Journal of Climate*, *25*(20), 6905 - 6929. Retrieved from <https://journals.ametsoc.org/view/journals/clim/25/20/jcli-d-11-00542.1.xml> doi: 10.1175/JCLI-D-11-00542.1
- Zhou, L., & Zhang, R.-H. (2023, March). A self-attention-based neural network for three-dimensional multivariate modeling and its skillful ENSO predictions. *Science Advances*, *9*(10), eadf2827. Retrieved 2023-12-08,

from <https://www.science.org/doi/10.1126/sciadv.adf2827>
10.1126/sciadv.adf2827

doi: